Journal of The Electrochemical Society

OPEN ACCESS

A Multilayer Doyle-Fuller-Newman Model to Optimise the Rate Performance of Bilayer Cathodes in Li Ion Batteries

To cite this article: E. C. Tredenick *et al* 2024 *J. Electrochem. Soc.* **171** 060531

Journal of The Electrochemical Society, 2024 **171** 060531

A Multilayer Doyle-Fuller-Newman Model to Optimise the Rate Performance of Bilayer Cathodes in Li Ion Batteries

E. C. Tredenick,[1,2,z] S. Wheeler,[2,3] R. Drummond,[1,4] Y. Sun,[2,3] S. R. Duncan,[1,2] and P. S. Grant[2,3]

[1]*Department of Engineering Science, University of Oxford, Oxford, OX1 3PJ, United Kingdom*
[2]*The Faraday Institution, Harwell Campus, Didcot, OX11 0RA, United Kingdom*
[3]*Department of Materials, University of Oxford, Oxford, OX1 3PH, United Kingdom*
[4]*Department of Automatic Control and Systems Engineering, University of Sheffield, Sheffield, S1 3JD, United Kingdom*

Bilayer cathodes comprising two active materials are explored for their ability to improve lithium-ion battery charging performance. Electrodes are manufactured with various arrangements of lithium nickel manganese cobalt oxide $Li[Ni_{0.6}Co_{0.2}Mn_{0.2}]O_2$ (NMC622) and lithium iron phosphate $LiFePO_4$ (LFP) active particles, including in two different discrete sub-layers. We present experimental data on the sensitivity of the electrode C rate performance to the electrode design. To understand the complex bilayer electrode performance, and to identify an optimal design for fast charging, we develop an extension to the Doyle-Fuller-Newman (DFN) model of electrode dynamics that accommodates different active materials in any number of sub-layers, termed the multilayer DFN (M-DFN) model. The M-DFN model is validated against experimental data and then used to explain the performance differences between the electrode arrangements. We show how the different open circuit potential functions of NMC and LFP can be exploited synergistically through electrode design. Manipulating the Li electrolyte concentration increases achievable capacity. Finally the M-DFN model is used to further optimize the best performing bilayer electrode arrangement by adjusting the ratio of the LFP and NMC sub-layer thickness.
 [DOI: 10.1149/1945-7111/ad5767]

Manuscript submitted January 17, 2024; revised manuscript received May 9, 2024. Published June 24, 2024.

Supplementary material for this article is available online

The electrification of vehicles and the replacement of the internal combustion engine are considered essential to meet targets for a net zero carbon economy, in the time frame 2035 to 2050.[1] To make this transition practical, economic, and to meet the expectations of customers for electric vehicles, improvements in electrical energy storage technologies are required. Currently, lithium-ion batteries (LIBs) are the most promising storage technology due to their high energy density (90–300 Wh/kg), energy efficiency (90%–100%), low maintenance, low self-discharge rate and relatively long lifespan (500–2,000 cycles).[2–4] The principal approach to improving LIBs has been through developments in the composition of the anode, cathode and/or electrolyte. However, existing chemistries such as graphite or graphite plus Si for the anode and $LiFePO_4$ (LFP) or $Li(NiMnCo)O_2$ (NMC) for the cathode are hard to displace in a fast growing market with increasingly commoditised prices, leading to generally reducing material costs. Moreover, there is resistance to adopt new cell chemistries because existing formulations have large and robust performance datasets that mitigate risk to manufacturers and end-users. An alternative approach to improve LIBs is to consider how well-characterised materials might be more efficiently utilised in a LIB by combining design and manufacturing innovations.[5]

Mass market LIB electrodes are a random mixture of the electrochemically active material (AM) particulate, a minority electrically conductive carbon (C) particulate, and a minority polymeric fraction that acts to bind (B) the particulates together in a $\sim$100 μm thick electrode. The binder also adheres the electrode to a thin metallic foil current collector to provide mechanical stability. A typical AM:C:B fraction is 96:2:2, and constitutes approximately 70% of the electrode volume with the remainder comprising tortuous, interconnected porosity that is subsequently filled with Li ion containing organic-based electrolyte. The electrode is formed by slurry casting and leads to an electrode structure that is a spatially random mixture of the solid components and pore space. The microstructure is isotropic with no deliberate variation from place to place. During LIB operation in regimes of practical interest, different parts of the through electrode thickness experience different local conditions due to the relatively slow mobility of charge carrying Li ions through the tortuous pore network. Some electrode regions charge rapidly and reach a full state of charge (SOC) early in the cycle, whereas other regions are barely charged.[6] This leads to cell performance far from the theoretical capacity, and accelerates degradation.[7] The principal reason for this inhomogeneous electrode response is the build up of steep through thickness Li ion concentration gradients, leading to a concentration gradient overpotential that is typically greatest furthest from the separator.[8,9]

To make better energy storage use of a greater fraction of the active particles over a larger proportion of the charge/discharge cycle (i.e. to adjust the local electrode microstructure to better suit the local mass transport and electrochemical conditions), non-random or tailored arrangements of the electrode materials have been explored. These include different AM particle diameters in different regions, both in graded and layered arrangements, different porosity fractions in different regions, or different proportions of AM:C:B from place to place.[6,7,10–16] For the specific case of electrode bilayers (an electrode made of two distinct sub-layers), studies have mainly focused on two layers of the same active material but with, for example, different particle diameters or volume fractions in each layer.[6,10–12] Generally, the rationale is to homogenise the rate of charge/discharge across the electrode thickness, by having a heterogeneous structure spatially tailored to avoid local over-provision, or under-provision, of Li ions, for energy storage reactions. For example, when a bilayer graphite negative electrode was used, cell capacity retention was improved compared with a chemically similar but homogeneous electrode.[6] Sub-layers with different particle sizes of NMC811 were used to form a positive electrode that improved overall capacity over a wide range of C rates,[11] and a similar approach improved capacity and slowed degradation compared with a homogeneous electrode comprised only of the larger NMC particles, and was similar to a homogeneous electrode comprising only the smaller NMC811 particles.[12] The slower rate of capacity degradation was likely due to reducing the time that some regions of the electrode were exposed to the highest voltages at the end of the charging curve, which drove solid

[z]E-mail: eloise.tredenick@eng.ox.ac.uk

electrolyte interphase (SEI) and other potentially capacity and lifetime degrading side reactions.[12] An LFP/$LiCoO_2$ based bilayer cathode showed a slightly improved capacity at higher C rates in discharge, while a LFP/Li[LiMnNi]O_2(LMO) bilayer cathode increased the specific capacity above a uniform LFP electrode at low C rate, but not at high C rate discharge.[17]

Modelling provides a cost effective method to explore different electrode arrangements including sub-layer arrangements, for example by varying either the particle size and/or the local porosity through the thickness of an electrode.[14,18–21] Like any electrode model, the models rely on the availability of data on how key properties vary with microstructuresuch as the local electrical conductivity or Li ion mobilityand require validation that relies on the manufacturability of the novel heteroelectrodes.

In this paper, we develop a numerical model of a bilayer LIB electrode, adapting the well-known Doyle-Fuller-Newman (DFN) or pseudo-two-dimensional (P2D) approach to describe the dynamics of electrodes with two discrete active material sub-layers. We apply the model to understand the underlying physical processes occurring during charge/discharge of bilayer electrodes. We explore the hypothesis that by optimising the position of different active material sub-layers, an overall electrode charging response can be achieved that is superior to any other combination of the same materials in the same proportion. We aim to maximise capacity at a given C rate, focusing on fast charging, and to improve the overall active material utilization. Finally, by achieving more efficient charging of the two materials in tandem, we confirm an overall improvement of the utilization of the active materials in a specific heteroelectrode arrangement, and we use the model to fine tune the bilayer arrangement to maximise capacity.

The cross-section of a bilayer electrode arrangement under consideration is shown in the plasma focused ion beam/scanning electron microscope (PFIB/SEM) back scattered electron (BSE) image in Fig. 1a with a corresponding schematic depiction of the arrangement in (b). The micrograph shows two distinct sub-layers. Adjacent to the current collector, the sub-layer is based on $LiFePO_4$ (LFP) as the active material, while in the upper layer, adjacent to the separator (separator not shown), the active material is $Li[Ni_{0.6}Co_{0.2}Mn_{0.2}]O_2$ (NMC622). The mean particle radius of the NMC is much larger than LFP,[9] and there are some cracks that developed due to calendering. The bilayer electrode was fabricated using two pass doctor blade coating, which in principle, has the potential to be industrially scalable.[6] The ratio of NMC:LFP thickness is approximately 50:50 and the total cathode thickness is 88 μm (i.e. each sub-layer is approximately 44 μm thick). This electrode arrangement is termed "NMC:LFP:CC" to indicate the LFP sub-layer is adjacent to the metallic current collector (CC). Also considered are "NMC-only" and "LFP-only" conventional single active material electrodes. Experimental charge/discharge data for the LFP-only and NMC622-only electrodes were used to validate the standard DFN model, and then NMC:LFP:CC bilayer experimental data was used to validate the Multilayer DFN (M-DFN) model. The NMC:LFP:CC bilayer arrangement was then explored in detail using the M-DFN model for different active material arrangements.

Multilayer DFN Model (M-DFN)

Governing equations.—The "standard" modelling approach to simulate the response of LIB electrodes and full cells has emerged as the pseudo-two-dimensional (P2D) or Doyle-Fuller-Newman (DFN) model.[8,22] The DFN model consists of a set of coupled partial differential equations (PDEs) in the form of nonlinear parabolic and elliptic PDEs, which consider both the electrode through-thickness, x, and the additional active material particle radius pseudo-dimension, r. We extend the DFN model by developing the "Multilayer DFN" model (M-DFN) to accommodate variations in electrode microstructure and properties through the thickness, and we formulate the model to describe any number of sub-layers with different electrochemically active particle properties. Compared with the standard DFN model, the M-DFN model for an electrode with two sub-layers roughly doubles the number of PDEs and variables solved, and requires extra boundary conditions between the two active materials.

Figure 2 shows the half-cell positive electrode M-DFN model domain. The cell is arranged as the Li counter electrode (CE), separator, two positive electrode sub-layers for NMC and LFP, and the current collector (CC). For the bilayer positive half-cell, $i \in \{1, 2\}$, where i is the index of each sub-layer in the electrode and p1 is NMC and p2 is LFP in this case (which can be extended if interested in a trilayer to 3 and further). The modelling domain, Ω, in Fig. 2 in terms of the electrode through-thickness direction, x, is: $0 < x < \ell_1$, $\ell_1 < x < \ell_2$, $\ell_2 < x < \ell_3$, $\ell_1 = L_s$, $\ell_2 = L_s + L_{p1}$, $\ell_3 = L_s + L_{p1} + L_{p2}$, where the lengths of the separator, p1 and p2 are L_s, L_{p1} and L_{p2}, respectively. The second pseudo-dimension is the spherical particle radius direction, r, which is solved for at each point in x, r_{p1} and r_{p2}, $0 < r_{p1} < R_{p1}$, $0 < r_{p2} < R_{p2}$. The length of each particle radius for p1 and p2, is R_{p1}

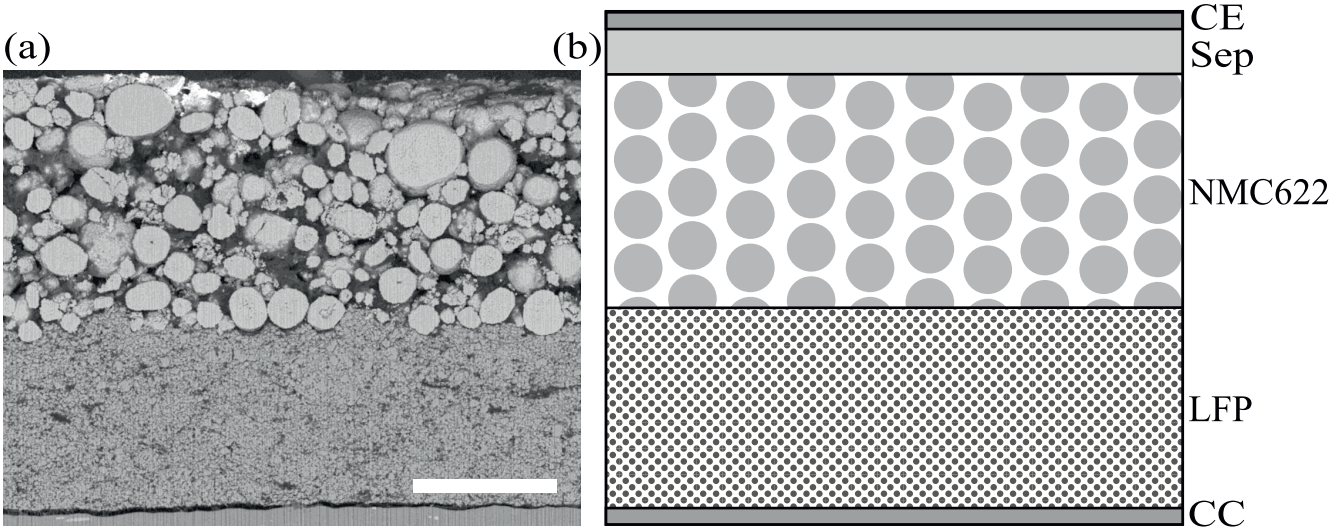

Figure 1. (a) Plasma focused ion beam/scanning electron microscope (PFIB/SEM) back scattered electron (BSE) image of a bilayer positive electrode for Li ion half-cell comprising a $LiFePO_4$ (LFP) sub-layer next to the Al current collector (CC) and a Li(NiMnCo)O_2 (NMC) sub-layer on top onto which the separator (Sep) and a Li counter electrode (CE) were added, and (b) a schematic representation of the arrangement. This arrangement is referred to as "NMC:LFP:CC", and the scale bar in (a) is 50 μm.

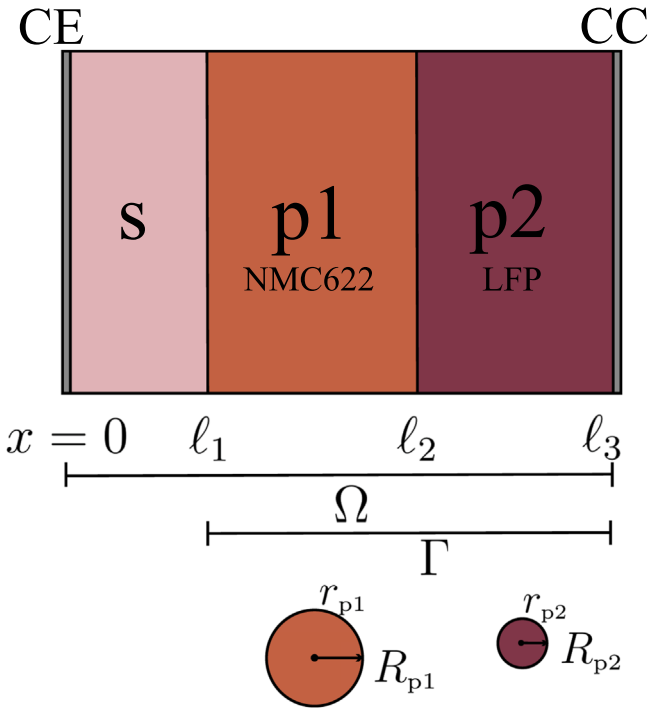

Figure 2. The M-DFN model domain, comprising Li counter electrode (CE), separator (s), positive electrode sub-layer p1 (NMC in this case), positive electrode p2 (LFP in this case), and current collector (CC). The domain, Ω, and sub-domain, Γ, that excludes the separator, are shown. There are three model compartments including (i) separator, (ii) positive one, and (iii) positive two. x is the electrode through-thickness direction and r is the active material particle radius direction. There are boundary conditions at $x = 0$, ℓ_1, ℓ_2 and ℓ_3.

Table I. Variables of the M-DFN model and $k \in${s,p}, where k is either the separator (s) or positive electrode (p).

Parameter	Description	Unit
$a_{\mathrm{p,i}}$	Reaction surface area per volume	1/m
$c_{\mathrm{e,k,i}}$	Concentration of Li ions in the liquid electrolyte	mol/m^3
$c_{\mathrm{s,p,i}}$	Concentration of Li ions in the solid particles	mol/m^3
$D_{\mathrm{e,k,i}}$	Diffusivity function in the electrolyte	m^2/s
$D_{\mathrm{e,bulk}}$	Bulk diffusivity function in the electrolyte	m^2/s
$J_{\mathrm{p,i}}$	Butler-Volmer reaction current density	A/m^2
$J_{0,\mathrm{p,i}}$	Exchange current density	A/m^2
$r_{\mathrm{p,i}}$	Particle radius direction	m
t	Time	s
$U_{\mathrm{p,i}}$	Open circuit potential (OCP)	V
V	Voltage	V
x	Direction through cell	m
$\kappa_{\mathrm{e,k,i}}$	Ionic conductivity function in the electrolyte	S/m
$\kappa_{\mathrm{e,bulk}}$	Bulk ionic conductivity function in the electrolyte	S/m
$\eta_{\mathrm{p,i}}$	Local overpotential	V
$\phi_{\mathrm{s,p,i}}$	Potential in the solid particles	V
$\phi_{\mathrm{e,k,i}}$	Potential in the liquid electrolyte	V

and R_{p2}. We define a variable I_{sign}, the sign of the applied current, which changes depending on whether the cell is being discharged or charged, as $I_{\mathrm{sign}} = -1$ for discharge, and $I_{\mathrm{sign}} = 1$ for charge.

The governing PDEs of the M-DFN model are as follows, with the variables described in Table I and key parameters given in Table II:

$$\frac{\partial c_{\mathrm{s,p,i}}}{\partial t} = \frac{1}{r_{\mathrm{p,i}}^2}\frac{\partial}{\partial r_{\mathrm{p,i}}}\left(r_{\mathrm{p,i}}^2\, D_{\mathrm{s,p,i}}\frac{\partial c_{\mathrm{s,p,i}}}{\partial r_{\mathrm{p,i}}}\right),\quad 0 < r_{\mathrm{p,i}} < R_{\mathrm{p,i}},\ \text{on}\ \Gamma,\ t > 0, \tag{1a}$$

$$-\frac{\partial}{\partial x}\left(-\sigma_{\mathrm{s,p,i}}\frac{\partial \phi_{\mathrm{s,p,i}}}{\partial x}\right) = a_{\mathrm{p,i}}\, J_{\mathrm{p,i}},\ \text{on}\ \Gamma,\ t > 0, \tag{1b}$$

$$\varepsilon_{\mathrm{e,p,i}}\frac{\partial c_{\mathrm{e,p,i}}}{\partial t} = -\frac{\partial}{\partial x}\left(-D_{\mathrm{e,p,i}}\frac{\partial c_{\mathrm{e,p,i}}}{\partial x}\right) + \frac{(1-t^+)\, a_{\mathrm{p,i}}\, J_{\mathrm{p,i}}}{F},\ \text{on}\ \Gamma,\ t > 0, \tag{1c}$$

$$\varepsilon_{\mathrm{e,s}}\frac{\partial c_{\mathrm{e,s}}}{\partial t} = -\frac{\partial}{\partial x}\left(-D_{\mathrm{e,s}}\frac{\partial c_{\mathrm{e,s}}}{\partial x}\right),\quad 0 < x < \ell_1,\ t > 0, \tag{1d}$$

$$\frac{\partial}{\partial x}\left[\kappa_{\mathrm{e,p,i}}\left(-\frac{\partial \phi_{\mathrm{e,p,i}}}{\partial x} + \omega\,\frac{\partial(\ln(c_{\mathrm{e,p,i}}))}{\partial x}\right)\right] = a_{\mathrm{p,i}}\, J_{\mathrm{p,i}},\ \text{on}\ \Gamma,\ t > 0, \tag{1e}$$

$$\frac{\partial}{\partial x}\left[\kappa_{\mathrm{e,s}}\left(-\frac{\partial \phi_{\mathrm{e,s}}}{\partial x} + \omega\,\frac{\partial(\ln(c_{\mathrm{e,s}}))}{\partial x}\right)\right] = 0,\quad 0 < x < \ell_1,\ t > 0. \tag{1f}$$

where $c_{\mathrm{s,p,i}}(r_{\mathrm{p,i}}, x, t)$, $\phi_{\mathrm{s,p,i}}(x)$, $c_{\mathrm{e,p,i}}(x, t)$, $D_{\mathrm{e,i}}(c_{\mathrm{e,i}})$, $\kappa_{\mathrm{e,p,i}}(c_{\mathrm{e,i}})$, $\phi_{\mathrm{e,i}}(x)$, $J_{\mathrm{p,i}}(c_{\mathrm{e,p,i}}, c_{\mathrm{s,p,i}}, \phi_{\mathrm{s,p,i}}, \phi_{\mathrm{e,p,i}}, U_{\mathrm{p,i}})$ and

$$\omega = \frac{2\,(1-t^+)\,R\,T}{F}. \tag{2}$$

Equation 1a describes Li ion mass transport with Fickian diffusion in the solid phase through the spherical particle including a constant solid particle diffusion coefficient, D_{s}. Equation 1b describes charge transport, which is based on Ohm's law for the solid phase current including particle surface reactions. Equation 1c describes mass transport in the liquid electrolyte with porous diffusion, which depends on a diffusivity function, D_{e}, that includes porosity and varies with concentration of the electrolyte, c_{e} (Eq. 7e and 7f). Equation 1d describes porous diffusion of Li ions in the electrolyte in the separator, and Eqs. 1e and 1f represent charge transport in the electrolyte with a modified form of Ohm's law and StefanMaxwell diffusion, where electrolyte conductivity, κ_{e}, which includes porosity, varies with concentration of the electrolyte, c_{e} (Eqs. 7g and 7h). The electrolyte diffusivity and conductivity, D_{e} and κ_{e}, are functions (Eqs. S1 and S2) of the electrolyte concentration, c_{e}, therefore Eqs. 1c–1f represent nonlinear transport.

The boundary conditions that hold for $t > 0$ are:

$$\left.\frac{\partial c_{\mathrm{s,p,i}}}{\partial r_{\mathrm{p,i}}}\right|_{r_{\mathrm{p,i}}=0} = 0,\ \text{on}\ \Gamma, \tag{3a}$$

$$\left.-D_{\mathrm{s,p,i}}\frac{\partial c_{\mathrm{s,p,i}}}{\partial r_{\mathrm{p,i}}}\right|_{r_{\mathrm{p,i}}=R_{\mathrm{p,i}}} = \frac{J_{\mathrm{p,i}}(R_{\mathrm{p,i}}, x, t)}{F},\ \text{on}\ \Gamma, \tag{3b}$$

$$\left.\frac{\partial \phi_{\mathrm{s,p1}}}{\partial x}\right|_{x=\ell_1} = 0, \tag{4a}$$

Table II. Model parameters, where p1 refers to NMC622 and p2 refers to LFP.

Parameter	Description	Unit	Value	Source
A	Electrode cross-sectional area	m^2	1.54×10^{-4}	Experiment
b_{p1}	Bruggeman tortuosity factor	—	1.6	24
b_{p2}		—	2.1	—
b_s		—	1.5	25
c_{e0}	Initial concentration of Li ions in electrolyte	mol/m^3	1000	Experiment
$c_{s,p1,0}$	Initial concentration of Li ions in solid particles, charge and discharge	mol/m^3	44 868, 13 366	S12
$c_{s,p2,0}$		mol/m^3	22 751, 29	S13
$c_{s,p1}^{max}$	Maximum concentration of Li ions in solid particles	mol/m^3	48 700	26
$c_{s,p2}^{max}$		mol/m^3	22 806	27
$D_{s,p1}$	Diffusivity of Li ions in solid	m^2/s	4×10^{-14}	Mean of data 28
$D_{s,p2}$		m^2/s	3×10^{-16}	—
F	Faraday constant	sA/mol	96 485.33	29
I	Current density	A/m^2	$I = I_c/A$	
I_c	Applied current for 1C	mA	5.76	Experiment
k_{p1}	Reaction rate constant	$m^{2.5}\ s^{-1}mol^{-0.5}$	1×10^{-10}	—
k_{p2}		$m^{2.5}s^{-1}mol^{-0.5}$	8×10^{-13}	—
L_{p1}	Thickness	μm	44.0	Experiment
L_{p2}		μm	44.0	Experiment
L_s		μm	16.0	Experiment
R	Universal gas constant	J/K/mol	8.314	
R_c	Contact resistance	$\Omega\ m^2$	1.5×10^{-3}	—
R_{p1}	Radius of particle	μm	4.94	9
R_{p2}		μm	0.43	9
T	Constant absolute reference temperature	K	293.15 (20 °C)	Experiment
U_0	Initial voltage, charge and discharge	V	3, 4.19	Experiment
t^+	Transference number of the electrolyte	—	0.37	30
$\varepsilon_{CBD,p1}$	Carbon binder domain volume fraction	—	0.11	—
$\varepsilon_{CBD,p2}$		—	0.11	—
$\varepsilon_{e,p1}$	Electrolyte volume fraction	—	0.31	Experiment and 9
$\varepsilon_{e,p2}$		—	0.263	Experiment and 9
$\varepsilon_{e,s}$		—	0.45	Experiment
$\sigma_{s,p1}$	Electronic conductivity in solid	S/m	5.0	Experiment
$\sigma_{s,p2}$		S/m	5.0	Experiment

$$-\sigma_{s,p1}\frac{\partial \phi_{s,p1}}{\partial x}\bigg|_{x=\ell_2} = -\sigma_{s,p2}\frac{\partial \phi_{s,p2}}{\partial x}\bigg|^{*}_{x=\ell_2}, \quad [4b]$$

$$\phi_{s,p2}(\ell_2, t) = \phi_{s,p1}(\ell_2, t)^{*}, \quad [4c]$$

$$-\sigma_{s,p2}\frac{\partial \phi_{s,p2}}{\partial x}\bigg|_{x=\ell_3} = -I\ I_{sign}, \quad [4d]$$

$$-D_{e,s}\frac{\partial c_{e,s}}{\partial x}\bigg|_{x=0} = -\frac{(1-t^+)\ I\ I_{sign}}{F}, \quad [5a]$$

$$-D_{e,s}\frac{\partial c_{e,s}}{\partial x}\bigg|_{x=\ell_1} = -D_{e,p1}\frac{\partial c_{e,p1}}{\partial x}\bigg|_{x=\ell_1}, \quad [5b]$$

$$c_{e,p1}(\ell_1, t) = c_{e,s}(\ell_1, t), \quad [5c]$$

$$-D_{e,p1}\frac{\partial c_{e,p1}}{\partial x}\bigg|_{x=\ell_2} = -D_{e,p2}\frac{\partial c_{e,p2}}{\partial x}\bigg|^{*}_{x=\ell_2}, \quad [5d]$$

$$c_{e,p2}(\ell_2, t) = c_{e,p1}(\ell_2, t)^{*}, \quad [5e]$$

$$\frac{\partial c_{e,p2}}{\partial x}\bigg|_{x=\ell_3} = 0, \quad [5f]$$

$$\text{Reference Potential:}\quad \phi_{e,s}(0, t) = 0, \quad [6a]$$

$$-\kappa_{e,s}\frac{\partial \phi_{e,s}}{\partial x}\bigg|_{x=\ell_1} = -\kappa_{e,s}\ \omega\ \frac{\partial(\ln(c_{e,s}))}{\partial x}\bigg|_{x=\ell_1} - I\ I_{sign}, \quad [6b]$$

$$\phi_{e,p1}(\ell_1, t) = \phi_{e,s}(\ell_1, t), \quad [6c]$$

$$\kappa_{e,p1}\left(-\frac{\partial \phi_{e,p1}}{\partial x} + \omega\ \frac{\partial(\ln(c_{e,p1}))}{\partial x}\right)\bigg|_{x=\ell_2} = \kappa_{e,p2}\left(-\frac{\partial \phi_{e,p2}}{\partial x} + \omega\ \frac{\partial(\ln(c_{e,p2}))}{\partial x}\right)\bigg|^{*}_{x=\ell_2}, \quad [6d]$$

$$\phi_{e,p2}(\ell_2, t) = \phi_{e,p1}(\ell_2, t)^{*}, \quad [6e]$$

$$\frac{\partial \phi_{e,p2}}{\partial x}\bigg|_{x=\ell_3} = 0. \quad [6f]$$

We utilize a pattern of boundary conditions to ensure continuity of concentration and potential in the form of either conservation of flux or values, "flux u_{p1}"="flux u_{p2}" or $u_{p2} = u_{p1}$, where u is ϕ_s, ϕ_e and c_e, at the p1/p2 boundary (ℓ_2), and these extra boundary conditions are indicated in Eqs. 3 to 6 with an "*". A full cell implementation of the M-DFN model is given in Eqs. S5–S11 and is shown schematically in Fig. S1. To achieve the reduced half-cell M-DFN model from the full cell model, the negative electrode/anode is replaced by a Li counter electrode[23] in Eq. 5a.

Functions and auxiliary equations for the reaction surface area per volume as a function of porosity and carbon binder domain porosity, the Butler-Volmer equation, local overpotential, diffusivity and conductivity of the electrolyte as a function of the bulk, porosity and tortuosity, and voltage including the resistance of the half-cell are:

$$a_{p,i} = \frac{3\,(1 - \varepsilon_{e,p,i} - \varepsilon_{CBD,p,i})}{R_{p,i}}, \text{ on } \Gamma, \quad [7a]$$

$$J_{p,i} = 2\,J_{0,p,i}\,\sinh\left(\frac{F\,\eta_{p,i}}{2\,R\,T}\right), \text{ on } \Gamma, \quad [7b]$$

$$J_{0,p,i} = k_{p,i}\,F\,\sqrt{c_{e,p,i}\,c_{s,p,i}(c_{s,p,i}^{max} - c_{s,p,i})}\,|_{r_{p,i}=R_{p,i}}, \text{ on } \Gamma, \quad [7c]$$

$$\eta_{p,i} = \phi_{s,p,i} - \phi_{e,p,i} - U_{p,i}|_{r_{p,i}=R_{p,i}}, \text{ on } \Gamma, \quad [7d]$$

$$D_{e,p,i}(c_{e,p,i}) = D_{e,bulk}(c_{e,p,i})\,\varepsilon_{e,p,i}^{\ b_{p,i}}, \text{ on } \Omega \text{ and } \delta\Omega, \quad [7e]$$

$$D_{e,s}(c_{e,s}) = D_{e,bulk}(c_{e,s})\,\varepsilon_{e,s}^{\ b_s}, \text{ on } \Omega \text{ and } \delta\Omega, \quad [7f]$$

$$\kappa_{e,p,i}(c_{e,p,i}) = \kappa_{e,bulk}(c_{e,p,i})\,\varepsilon_{e,p,i}^{\ b_{p,i}}, \text{ on } \Omega \text{ and } \delta\Omega, \quad [7g]$$

$$\kappa_{e,s}(c_{e,s}) = \kappa_{e,bulk}(c_{e,s})\,\varepsilon_{e,s}^{\ b_s}, \text{ on } \Omega \text{ and } \delta\Omega, \quad [7h]$$

$$V = \phi_{s,p2}(\ell_3, t) + R_c\,I\,I_{sign}. \quad [7i]$$

In Eq. 7a, which describes the reaction surface area per volume, the partial obscuring effect of the carbon binder domain (CBD) that tends to coat the active particles is included, by reducing the total surface area available for intercalation/de-intercalation reactions. The electrolyte diffusivity, D_e, and conductivity, κ_e, are included as functions in Eqs. 7e, 7f, 7g, 7h and Eqs. S1, S2, while D_s and σ_s are constants.

The initial conditions are:

$$c_{s,p,i}(r_{pi}, 0) = c_{s,p,i,0}, \text{ on } \Gamma \text{ and } \delta\Gamma, \quad [8a]$$

$$\phi_{s,p,i}(x, 0) = U_{p,i}, \text{ on } \Gamma \text{ and } \delta\Gamma, \quad [8b]$$

$$c_{e,k,i}(x, 0) = c_{e0}, \ k \in \{s,p\}, \text{ on } \Omega \text{ and } \delta\Omega, \quad [8c]$$

$$\phi_{e,k,i}(x, 0) = 0, \ k \in \{s,p\}, \text{ on } \Omega \text{ and } \delta\Omega, \quad [8d]$$

which describes the initial, constant Li ion concentration in the particles in both the r (particle scale) and x (electrode scale) directions. The potential in the active material, ϕ_s, is calculated based on the open circuit potential (OCP), U_p (Eqs. S12 and S13), while the Li ion concentration of the electrolyte, c_e, is assumed initially constant through x, and the potential in the electrolyte, ϕ_e, is zero.

Numerical solution procedure.—The M-DFN model, comprising Eqs. 1–7, is non-dimensionalised and solved numerically, using a finite volume approach, by discretising the PDEs on a uniform mesh using second order central differences to approximate the spatial derivatives, along with averaging of the diffusivity and conductivity functions (Eqs. 7e, 7f, 7g), at the control volume faces. The resulting system of ordinary differential equations is solved using "ode15s" including a mass matrix, within MATLAB® 2022b[31] on a desktop Macintosh (MacBook Pro, Monterey, v 12.4, M1 2020, 16GB, 256GB, 64 bit). The MATLAB M-DFN code simulations are relatively fast and the timings for a 1C discharge are shown in Table III. The open-source code for the uniform cells is available online (https://github.com/EloiseTredenick/DFN-P2D-Uniform-Matlab-NMC-LFP-LiIon-Batteries).

The unknown parameters required for the M-DFN model were obtained by manually fitting experimental data from uniform LFP and NMC half-cells and a NMC:LFP:CC half-cell at 0.1C charge, which were then further fine-tuned for a 3C charge. These parameters were then kept fixed for simulations at all C rates. The model parameters are shown in Table II and are a mixture of those taken from well-cited literature, from the experimental setup, or by fitting, as indicated by "-". The fitted tortuosity for the LFP sub-layer, b_{p2} was similar to those found elsewhere[9] and reaction rates, k_{p1} and k_{p2} were similar to those found elsewhere.[26,32,33] The mass and specific capacity of the NMC:LFP:CC half-cell are given in Table IV and were used to convert the model results as a function of time (in seconds), to capacity (in mAh/g) and normalised capacity, using Eq. S3.

Table III. Execution times of the M-DFN model code in MATLAB® 2022b[31] for a 1C discharge. The number of mesh nodes, N, in the particle radius, r, are shown, N_{rp1}, N_{rp2}, along with the nodes in each subdomain in x for the separator, p1 and p2, N_{sep}, N_{xp1}, N_{xp2}. N_{rp1} = 7 and 3 are suitable for testing only.

N_{rp1}	N_{rp2}	N_{sep}	N_{xp1}	N_{xp2}	States	Wall time
29	35	19	27	27	1,800	0.78 min
7	11	7	11	11	242	2.81 s
3	5	3	5	5	60	0.56 s

Experimental

Electrode fabrication.—Electrodes comprised NMC622 (BASF, Germany) and/or LFP (MTI, USA), carbon additive (C65, Imerys, UK), and polyvinylidene fluoride binder (PVDF, Solef 5130, Solvay, UK). Active materials and carbon conductive additive were dried overnight at 120 °C under vacuum. A 3wt% PVDF in 1-Methyl-2-pyrrolidinone (NMP, Sigma) solution was produced by stirring overnight. The electrode slurry was then produced by mixing the 3wt% PVDF in NMP solution with the active material and carbon conductive additive using a planetary mixer (Thinky ARE-250). Extra NMP was added to achieve the appropriate viscosity. Solid material mass fractions (active material: carbon additive: binder) were 96:2:2 for the NMC slurries and 92:4:4 for the LFP slurries, targeting an electronic conductivity of 5 S/m. The solid content fractions were approximately 60% for the NMC slurries and 40% for the LFP slurries. Electrode slurries were cast onto carbon-coated Al foil (MTI, 18 μm thickness) using a doctor blade and drawdown table. The doctor blade gap was adjusted to produce the electrode layer of appropriate areal loading and the table was heated to 70 °C to dry the electrode. For uniform electrodes, a single doctor blade pass was used. For bilayer electrodes, the first layer was cast and dried before casting the second layer directly on top. The electrode areal loading was measured by averaging over several 14 mm diameter disks punched from the electrodes. Electrodes were calendared to a thickness that resulted in a porosity of 30% for the uniform electrodes, and approximately 35% and 25% for NMC and LFP in the bilayer. Electrodes disks with a diameter of 14 mm were

Table IV. Experimental information for the NMC:LFP:CC half-cell bilayer electrode. The cathode mass excludes the separator and current collector mass.

Description	Value
Cathode electrode mass	0.0351 g
Specific capacity at 0.05 C (experimental and theoretical)	165 mAh/g
Specific areal capacity (theoretical—calculated)	3.74 mAh/cm^2
Min Voltage	2.5 V
Max Voltage	4.2 V

punched from the electrode sheet before drying at 120 °C under vacuum overnight and bringing into an Ar-filled glove box (Mbraun, $H_2O < 0.1$ ppm, $O_2 < 0.1$ ppm).

Electrochemical cell preparation.—Electrochemical cells were prepared in an Ar-filled glove box (MBRAUN, $H_2O < 0.1$ ppm, $O_2 < 0.1$ ppm) using a Li metal counter electrode, 16 μm separator (H1609, Celgard) and 1 M lithium hexafluorophosphate ($LiPF_6$) in ethylene carbonate (EC): ethyl methyl carbonate (EMC) (30:70 wt %) with vinylene carbonate (2 wt%) electrolyte (ELYTE). Three-electrode cells (PAT-Cell, EL-Cell) were prepared with a Li metal counter electrode, Li reference electrode and the same electrolyte. The three-electrode arrangement enabled more accurate control of the working electrode voltage, avoiding the impact of polarization from the counter electrode,[34] which becomes more significant as the C rate increases. Figure S3 shows the resulting three-electrode normalised charge capacity data at 1, 2, 3 and 4C for NMC:LFP:CC, NMC-only and LFP-only electrodes. For completeness, Fig. S4 shows two-electrode charge and discharge curves for the NMC:LFP:CC electrode at 0.1, 1 and 2C.

Electrochemical testing.—Coin cells were tested using a battery cycler (LBT21084, Arbin) while three-electrode cells were tested in a potentiostat (VSP, BioLogic). Formation cycling consisted of two cycles at 0.05 C and two cycles at 0.1 C. The charging and discharging protocols were constant current (CC) with upper and lower voltage cut-offs at 4.2 V and 2.5 V, respectively. All testing was carried out in a temperature-controlled environment at 20 °C.

Electronic conductivity measurement.—Electrodes were produced in the same manner as described above but cast onto an electrically insulating polyethylene terephthalate (PET) substrate. In-plane conductivity measurements were performed using a four-point probe (Ossila, UK).

Open circuit potential (OCP).—The experimental OCP profiles of NMC-only and LFP-only half-cells are shown in Figs. S2a and S2b, respectively. The NMC profile is gently sloping over the voltage range, while the LFP experimental data has a distinct plateau at 3.413 V, and both consistent with the large body of similar data for these well-characterised materials.

Results and Discussion

M-DFN Model.—Figures 3a to 3e shows comparisons of the M-DFN model with experimental data for 0.1, 1, 2, 3 and 4C charge, as a function of normalised capacity. Figure 3f shows the simulated discharge curves for 0.1, 1, 2, 3 and 4C, together with experimental data for 0.1C. The fit of the M-DFN model compared to the experiment data is acceptable at each C-rate considered, with the model able overall to capture both the measured profile shape and the capacity at the terminal voltage. For both discharge and charge, the NMC portion of the profile had the greatest contribution to the overall voltage profile because of its higher intrinsic capacity. Li ions in NMC and LFP particles delithiated/lithiated (charge/discharge) separately and sequentially, most distinctly at low C rates, because of the difference in their OCP curves (Fig. S2). As shown in Fig. 3, distinguishing between LFP and NMC portions of the profile became progressively more difficult as the C rate increased. This arose because charging the LFP sub-layer required a progressively higher overpotential due to the increasing charge transfer resistance and concentration polarization due to through thickness solid Li ion concentration gradients, such that the applied voltage for LFP charging became high enough to also start charging the NMC. This is described in more detail below.

Figure 3f shows a 1C discharge curve of the M-DFN model of a NMC:LFP:CC bilayer electrode. The profile shape can be recognised as a superposition of the NMC and LFP OCP profiles shown in Fig. S2. The first part of the discharge profile, which had a gently reducing voltage down to ~3.2 V was attributed to the lithiation of Li ions in the NMC sub-layer, while the second plateau portion indicated the lithiation of Li ions from the LFP sub-layer and occurred only once the NMC sub-layer was largely discharged.

The M-DFN model allows investigation of internal electrode dynamics not readily accessible by experiment, such as the spatially resolved particle surface reactions, Li concentrations in the active particles and electrolyte, and the potential in the active material and electrolyte. Figures 4a, 4b show the normalised active particle surface Li concentration as a function of position and time, for the NMC sub-layer and LFP sub-layer, respectively, for the NMC:LFP:CC electrode during a 1C discharge. At the start of the discharge ($t = 0$) the Li concentration was flat (black). The concentration of Li ions then increased with time: (a) uniformly across the NMC sub-layer, and (b) with a gradient across the LFP sub-layer, as reported elsewhere.[35] Regions of LFP Li concentration closest to the current collector took the longest time to begin discharging and were complete only after the NMC sub-layer and other regions of the LFP sub-layer were fully discharged. The NMC was fully discharged before most of the LFP started to discharge.

For the same electrode and condition, Fig. 5 shows the normalised active particle surface Li concentration, in this case as a function of time. The Li concentrations are taken from active particles at the four through-thickness positions (i) to (iv) shown in Fig. 4. The NMC Li concentration, regardless of position at (i) or (ii), increased linearly up to 1,900 s and then plateaued, while for LFP, the Li concentration at (iii) and (iv) remained flat until 1,900 s, and then increased, more slowly in regions closer to the CC. As described earlier, Li ions lithiated first into NMC and then later into LFP because the local voltage required for discharge was first achieved for the NMC sub-layer (as given by the OCP curve (Fig. S2a)). Only after 1,900 s did the local voltage reach that required for LFP discharge, as given by the OCP curve in Fig. S2b. For both the NMC and LFP sub-layers, the Li concentration gradients across the particle radius were minimal (profiles not shown for brevity).

For the same electrode and condition, Fig. 6 shows the Li concentration profile in the electrolyte through the electrode thickness with time. At the start of discharge, the Li concentration profile was flat (black) and set to 1,000 mol/m^3. As time progressed, a "see-saw" profile developed, where the Li concentration in the separator and NMC sub-layer increased, while the concentration in the LFP sub-layer adjacent to the current collector decreased. Towards the end of the discharge, the profile began to flatten once again. To visualise these electrode dynamics differently, Fig. 7 replots the electrolyte Li concentration as a function of time at the four locations (i) to (iv) in Fig. 6. For all points, there were relatively small changes in Li concentration between 0 and 1,900 s when only the NMC was lithiating. However, after ~1,900 s, when the LFP began to lithiate, the profiles separated, again with greater spatial variations in the LFP sub-layers. The Li concentration in the electrolyte in the LFP sub-layer near the current collector reached a minimum of approximately 600 mol/m^3.

Numerical Experiments.—The M-DFN model was then used to explore the factors governing the behavior of different electrode

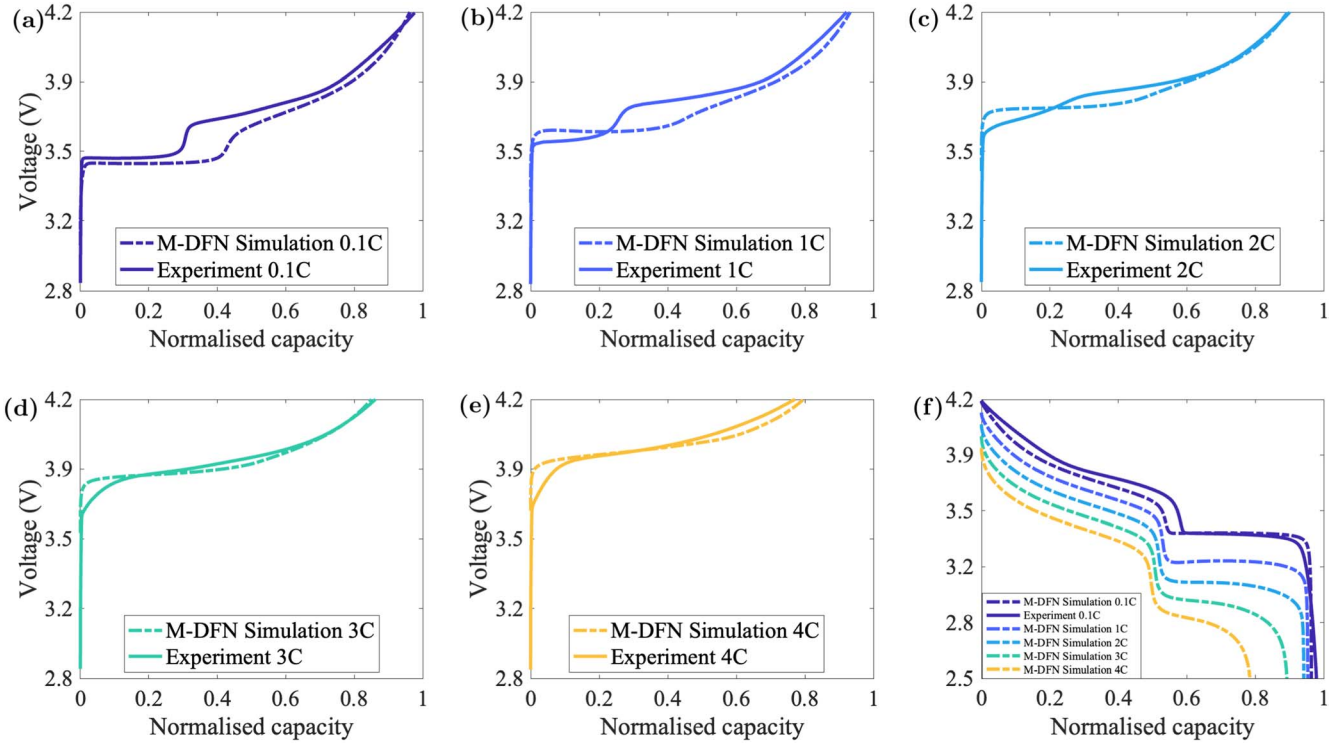

Figure 3. Comparison of the M-DFN model for a NMC:LFP:CC electrode (dashed lines) with experimental data (solid lines) for voltage as a function of normalised capacity (achieved capacity (mAh/g)/specific capacity (165 mAh/g)). Charge at 5 different C rates of (a) 0.1, (b) 1, (c) 2, (d) 3 and (e) 4 C, and (f) simulated and experimental discharge data.

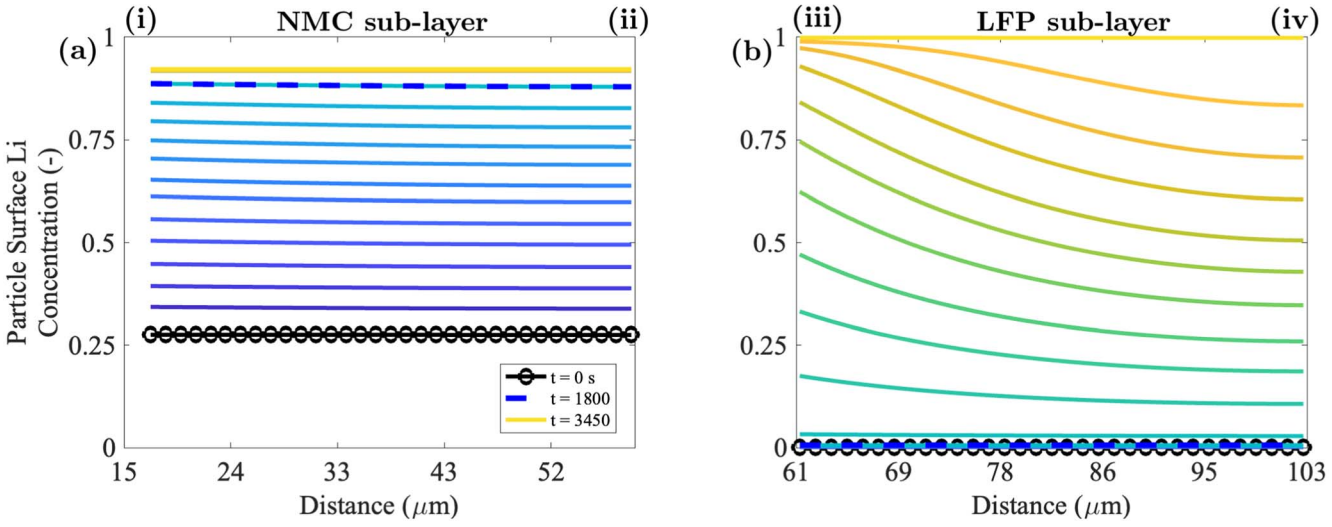

Figure 4. M-DFN simulations for a 1C discharge for a NMC:LFP:CC bilayer electrode. The plots are the normalised particle Li surface concentration ($c_{s,p,surf}/c_{s,p}^{max}$) of the (a) NMC and (b) LFP particles as a function of distance from the Li counter electrode/separator interface, and discharge time. The initial condition at the start of discharge ($t = 0$ s) is shown in black, the mid time (t=1,800 s) is shown as dashed blue and the final solution at the end of discharge (t=3,450 s) is shown in orange. The concentrations at the boundary conditions (i) to (iv) are replotted in Fig. 5.

conditions and arrangements. First, the M-DFN model was applied over a wide range of charge and discharge C rates for the same NMC:LFP:CC arrangement used in Figs. 4 to 7. Figure 8a shows simulated charging curves for the NMC:LFP:CC arrangement at a range of C rates, indicating a progressive loss of capacity at the terminal charging voltage of 4.2V. This is shown more clearly in Fig. 8b including terminal capacity as a function C rate. Capacity reduced steadily to 5C, reaching approximately 72% of the capacity at 0.05C, after which capacity reduced more rapidly. Figures 8c and 8d show similar data for the case of discharge, but now with a less marked reduction in capacity with increasing C rate after 2.5C. The trend of decreasing capacity with increasing C rate agrees with those described elsewhere for uniform composition electrodes.[36,37] By examining similar plots to those shown in Figs. 4 to 7 (not shown for brevity), the progressive drop in discharge capacity was identified as principally due to Li concentration depletion in the electrolyte in the LFP sub-layer close to the current collector, leading to under utilization of some of the LFP, as well as NMC, particles. The shape of the discharge/charge curves also changed, with the sharp transition from NMC to LFP discharge becoming progressively blurred as NMC and LFP particles charged or discharged increasingly in parallel rather than sequentially. Figure 9 shows a similar

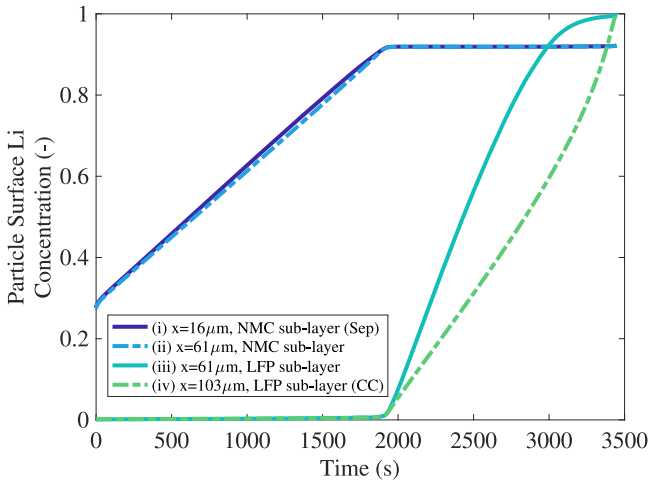

Figure 5. The normalised particle Li surface concentration ($c_{s,p,surf}/c_{s,p}^{max}$) of NMC and LFP particles as a function of time for a 1C discharge in the NMC:LFP:CC bilayer electrode replotted from Fig. 4 at the boundary conditions (i) to (iv). The Li concentrations are taken from particles at different through-thickness positions: (i) from NMC particles at the NMC sub-layer/separator interface (16 μm); (ii) from the NMC particles at the centre of the electrode (61 μm); (iii) from LFP particles also at the centre of the electrode (61 μm) and (iv) from LFP particles at the LFP/current collector interface (103 μm).

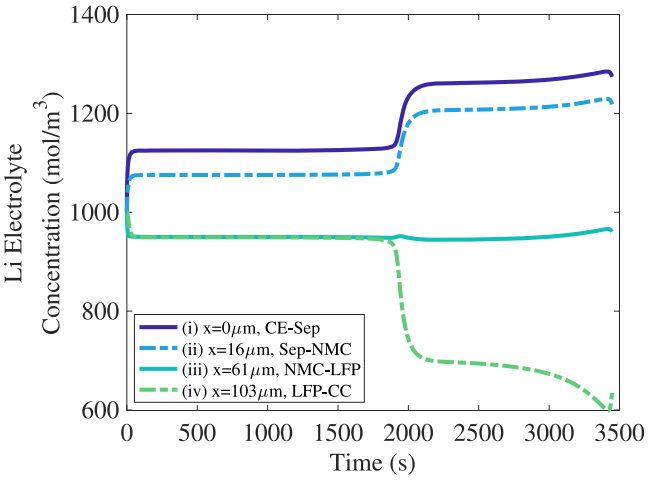

Figure 7. The simulated Li concentration in the electrolyte, c_e, as a function of time, for a 1C discharge and NMC:LFP:CC arrangement, replotted from Fig. 6, at the (i) counter electrode/separator interface (0 μm); (ii) the separator/NMC sub-layer interface (16 μm); (iii) NMC sub-layer and LFP sub-layer interface (61 μm); and (iv) the LFP sub-layer close to the current collector (103 μm).

effect of C rate on discharge capacity in Fig. 8c but in this case is due to an increase in the overall electrode thickness from 58 μm up to 160 μm, while keeping the NMC:LFP sub-layer thickness ratio constant, at a 1C discharge.

As the electrode thickness increased, there was a corresponding increase in theoretical specific areal capacity for 2.5 to 6.8 mAh/cm^2. Figure 9a shows the shape of the profiles remained similar as the rate changed and when the capacity was normalised by the specific areal capacity at 0.05C, Fig. 9b shows that the discharge curves approximately overlaid one another, except for the thickest 160 μm electrode in which localised electrolyte depletion, especially in the LFP sub-layer, became a capacity limiting factor.

Fast Charging and the Influence of Electrode Architecture.— So far only the NMC:LFP:CC 50:50 thickness ratio bilayer electrode arrangement has been considered, both in the M-DFN model and by experiment. To investigate the hypothesis that there is an optimum layered arrangement of NMC and LFP sub-layers, with a focus on fast charging at 3C, a number of other arrangements are now investigated. We also compare the NMC:LFP:CC bilayer electrode performance to NMC-only and LFP-only electrodes, additional examples that were fabricated with similar areal capacities. The corresponding model parameters are given in Table S2 and Table V. The single active material electrode parameters were obtained by first starting with the validation parameters from Table II, and then adjusting until differences were minimised, resulting in some changes including the reaction rate for LFP and NMC, k_p, the tortuosity for LFP, b_{p2} and the contact resistance, R_c.

Figure 10a shows a comparison of the experimental and simulated voltage profiles as a function of normalised capacity for NMC:LFP:CC, NMC-only and LFP-only electrodes at 3C charge. Once again, the model provided good agreement with experiment, capturing the shape of the profiles and the capacity at the terminal voltage to within ~1% (Table V). The NMC:LFP:CC electrode began charging at a voltage between that of the LFP and NMC-only

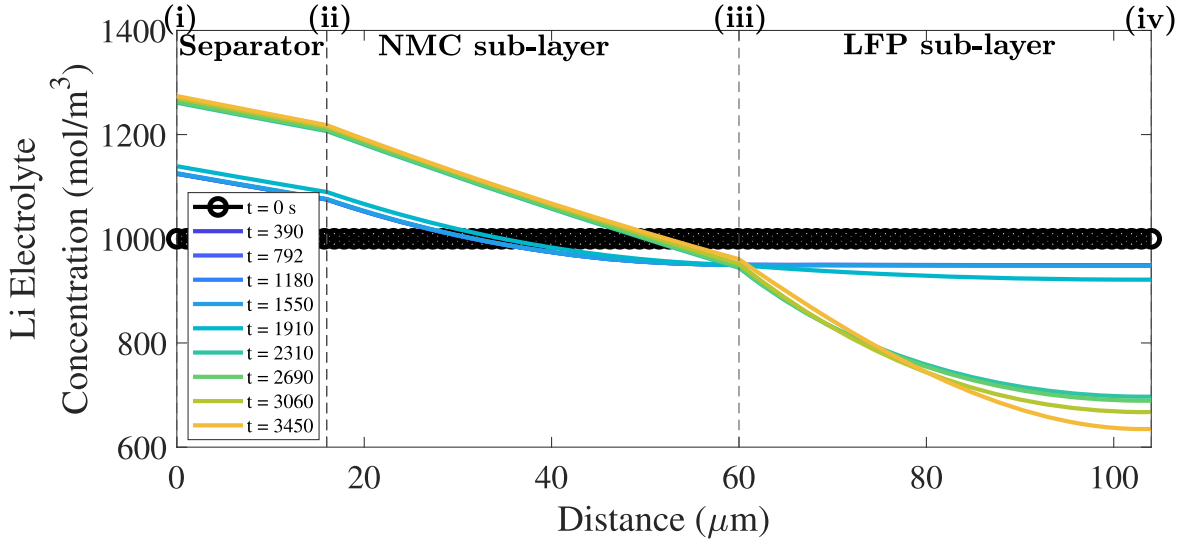

Figure 6. The simulated concentration of Li in the electrolyte, c_e, for a 1C discharge of a NMC:LFP:CC electrode. The concentration profile at the start of discharge ($t = 0$ s) is black and the final profile at the end of discharge ($t = 3{,}450$ s) is orange. The concentration at the boundary conditions (i) to (iv) are replotted in Fig. 7.

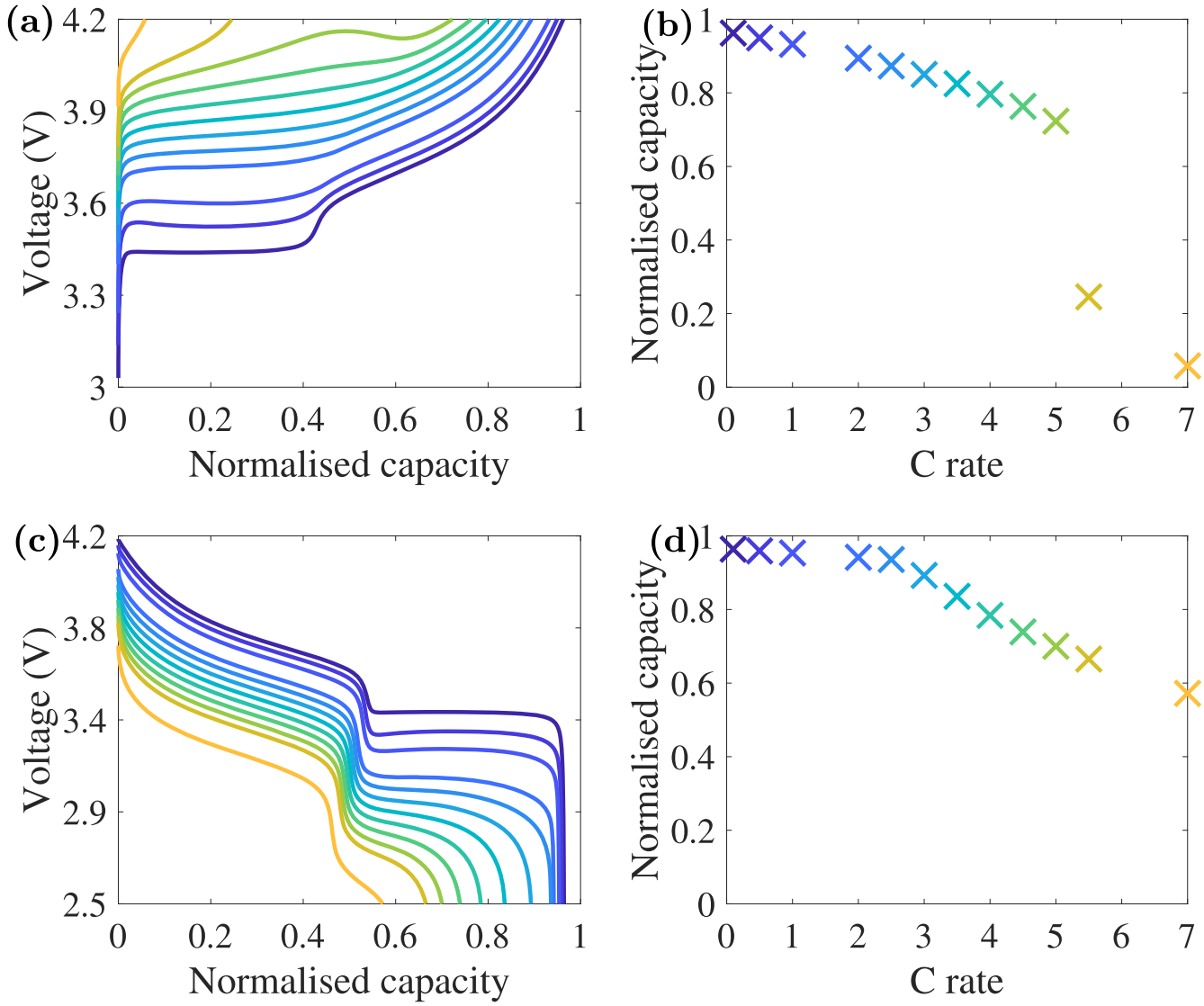

Figure 8. Simulated charge and discharge plots between 0.1 and 7C for a NMC:LFP:CC electrode. (a) charging and (c) discharging voltage as a function of normalised capacity (achieved capacity/specific areal capacity at 0.05C) for a range of C rates, and the corresponding (b) charge capacity at 4.2 V and (d) discharge capacity at 2.5 V as a function of C rate.

electrodes. As seen previously at 2, 3 and 4C in Fig. 3, the NMC and LFP portions of the NMC:LFP:CC electrode charged together, and there was no separation between the LFP voltage plateau and sloping NMC profile. The capacity achieved at the terminal voltage of 4.2 V for both the simulations and experiments is shown in Table V and Fig. 10b with good agreement, and the NMC:LFP:CC electrode produced the highest normalised capacity of 85%, which was 6.3% higher than NMC-only and 5.6% higher than LFP-only electrodes. Although these relatively small differences in experimental capacity between electrodes were resolved successfully by the model, relatively small experimental capacity differences could be due to inherent variability that can be a feature of coin cells. However, we note that capacity measurements were taken for a wide range of electrode arrangements and electrochemical conditions, and the resulting trends were always smooth and monotonic (see for example Fig. S3). Therefore, if there were uncontrolled variability in the measured capacities, it was significantly smaller than the condition-to-condition differences that are the focus of the work.

In Fig. S3 for a 4C charge, the NMC:LFP:CC bilayer experimentally achieved 11.2% and 14.8% higher capacity than LFP-only and NMC-only, respectively. Figure S5 is the charge-discharge simulation cycle at 3C, indicating that the bilayer discharge capacity was 2.6% and 2.2% higher than NMC-only and LFP-only, respectively. Long-term cycling is not the focus of the current work although preliminary data suggests the capacity differences between the electrodes on charge is maintained.

Figure S6 shows the corresponding normalised Li particle concentration for the NMC:LFP:CC, NMC-only and LFP-only electrodes at a 3C charge as a function of electrode thickness at different times during charge. Figures S6a and S6c show that for NMC sub-layer and the NMC-only electrode respectively, there were similar fractions of NMC utilization. In contrast, the LFP sub-layer shown in (b) was fully charged, whereas the LFP-only electrode shown in (d) had a small fraction of under utilised LFP, due to electrolyte depletion as shown in the corresponding Li concentration in the electrolyte plot in Fig. S7.

Having established the robustness and fit of the model to experiment, the model was used to explore different sub-layer thicknesses for a 4.5C charge, as this was close to peak bilayer performance (Fig. 8). The range of NMC sub-layer thicknesses ranged from 11 μm to 69 μm representing a range of thickness fractions of 10% to 93%. Figure 11 shows the capacity at 4.2 V as a function of the NMC sub-layer thickness, and the voltage as a function of capacity is shown in Fig. S8. To maintain a charge rate of

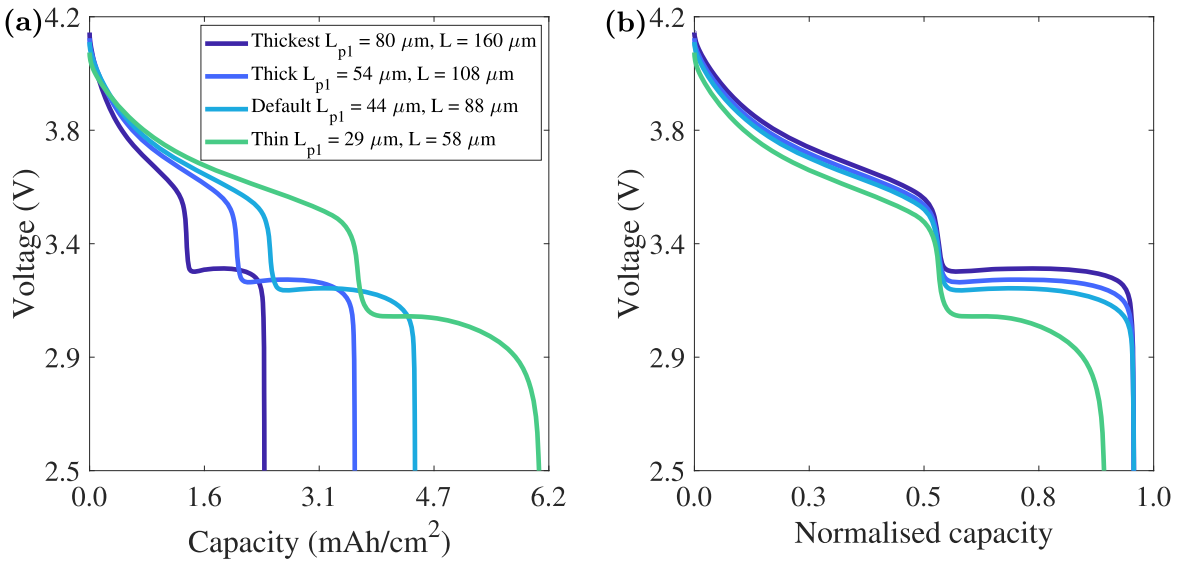

Figure 9. Simulated NMC:LFP:CC electrode discharge response for a range of thicknesses at 1C. The NMC to LFP sub-layer ratio was kept constant at 50:50. The simulation parameters were the same as the validation (Fig. 3) unless stated otherwise in Table S1. (a) is replotted in (b) after normalising by the specific areal capacity at 0.05C.

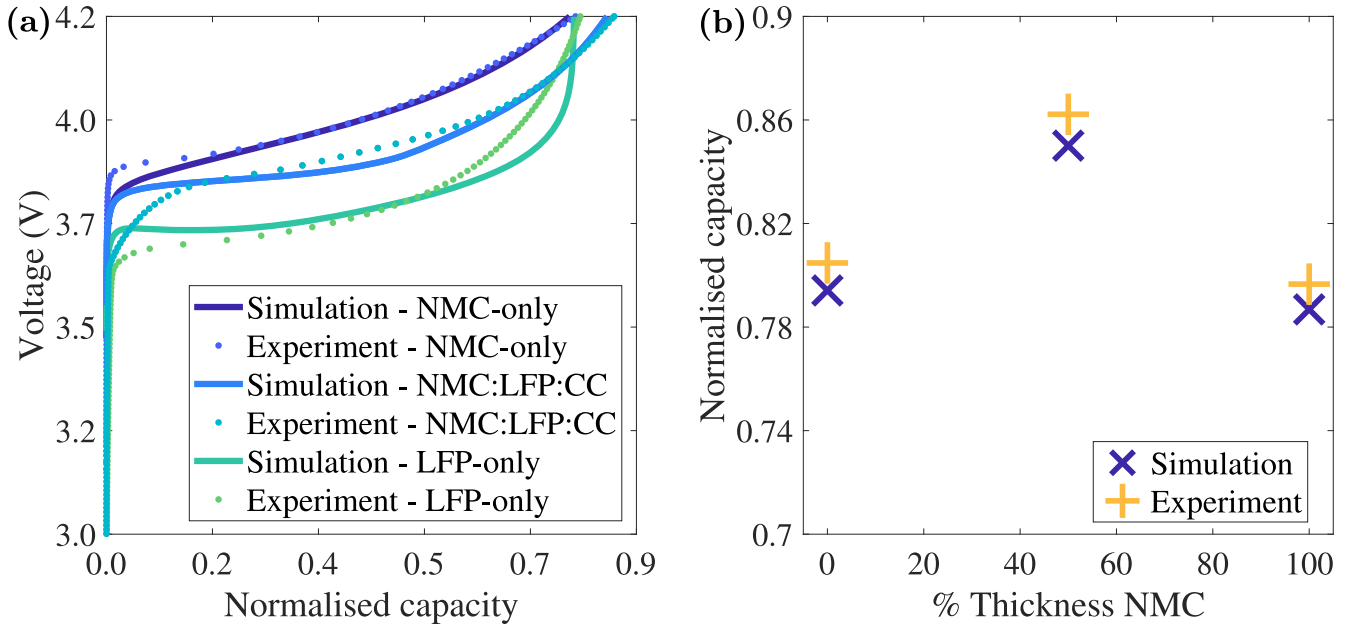

Figure 10. Comparison of voltage verses capacity from the M-DFN model and experiment for the NMC:LFP:CC bilayer, NMC-only, and LFP-only electrodes at 3C charge. Achieved capacity was normalised by the specific capacity at 0.05C (mAh/g).

Table V. The specific capacities at 0.05C, and achieved capacities at 4.2 V during a 3C charge, for the M-DFN model and experiment, for the NMC:LFP:CC bilayered, LFP-only, and NMC-only electrodes, respectively.

			Units	NMC:LFP:CC	LFP-only	NMC-only
Thickness			μm	44: 44 (88 total)	108	64
Specific capacity at 0.05C	Areal		mAh/cm^2	3.74	3.57	3.37
	Mass		mAh/g	165	150	175
Achieved capacity at 4.2 V and 3C	Areal	Simulated	mAh/cm^2	3.19	2.84	2.65
	Mass	Simulated	mAh/g	140.3	119.1	137.7
		Experiment	mAh/g	142.3	120.7	139.4
Normalised achieved capacity at 4.2 V and 3C		Simulated	%	85.0	79.4	78.7
		Experiment	%	86.2	80.5	79.7

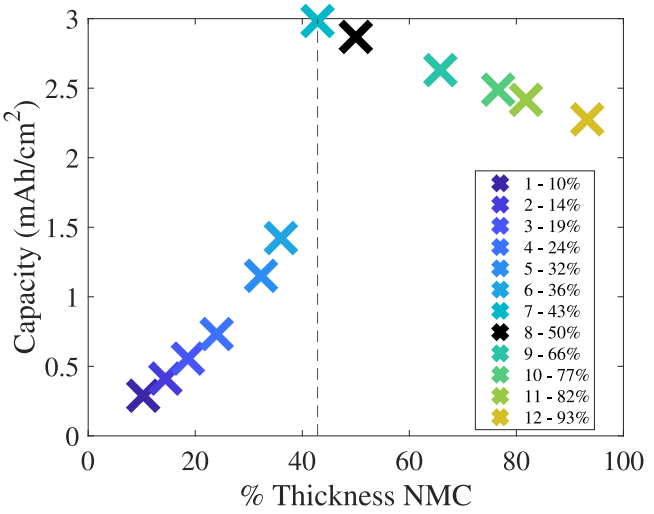

Figure 11. Simulated capacity at 4.2 V for a 4.5C charge for a range of NMC sub-layer thicknesses. The default NMC:LFP 50:50 thickness ratio arrangement is shown by the black cross. The corresponding voltage plots are shown in Fig. S8.

4.5C and consistent specific areal capacities (~3.74 mAh/cm^2) for each electrode as the proportion of NMC to LFP changed, the overall electrode thickness was adjusted, while all other parameters remained the same, as shown in Table S3. Figure 11 shows that for a 4.5C charge, out of the 12 cases studied (Table S3), a 43% NMC thickness provided the highest capacity of 3 mAh/cm^2, fractionally higher than the default 50% case of 2.9 mAh/cm^2. Increasing the relative thickness of the NMC sub-layer and total electrode thickness beyond the optimum (91 μm) reduced the overall capacity, albeit gradually, while reducing the relative thickness reduced capacity relatively sharply.

Figure 12 shows the state of charge (SOC) through the electrode thickness at the end of the 4.5C charge and the terminal voltage of 4.2 V, for the 12 arrangements. When the NMC sub-layer was thinner than the optimal (cases 1 to 6), overall capacity reduced because of more under utilization of the LFP sub-layer, caused by an increased fraction of local electrolyte depletion, seen in plots similar to those shown in Figs. 4 to 7 (not shown for brevity), along with under utilization in the NMC sub-layer. When the local Li concentration in the electrolyte in the separator approached zero, the applied voltage increased rapidly to the cutoff voltage causing the charging to cease early. Figure 12 shows that the active material closer to the separator reached a high SOC faster than material near the current collector and when the NMC sub-layer was thicker than the optimum (cases 8 to 12), capacity was again reduced because there was proportionally less of the relatively readily charged LFP, as shown in Fig. 12b.

Figures 13a to 13c shows the Butler-Volmer reaction current densities for bilayer cases 4, 8 and 12 from Table S3, and corresponding to the cases in Fig. 11 for the second thinnest, 50% and thickest NMC sub-layer cases, throughout the 4.5C charge. Dimensionless current density, $\bar{J}$, is shown as a function of time and position. The NMC sub-layers displayed small variations in current density over space and time, and did not finish reacting, i.e. the NMC failed to reach 100% SOC in all cases (100% SOC is indicated by a black region ($\bar{J} = 0$)). In contrast, the LFP sub-layers showed a peak in reaction current density that occurred at different times and positions corresponding to the travelling front of increasing Li particle concentration, that moves through the electrode due to the plateau in the OCP of LFP, as previously described for Fig. 4. In Fig. 13a, when the NMC sub-layer was relatively thin, charging stopped at around 158 s with the LFP sub-layer yet to reach 100% SOC. For the conditions in Figs. 13b and 13c, the LFP sub-layer finished reacting and was fully charged at the terminal voltage. In Fig. 13b for the 50% case, the terminal charging voltage was reached at 630 s, which was the longest overall charge time, and gave the highest overall capacity (Fig. 11). Considering cases 4, 8 and 12, the difference in electrode thickness is significant (100 μm, 88 μm and 74 μm, respectively) and when the electrode thickness is greater than the optimal of 91 μm, this limits the capacity at 4.5C. In Fig. 13c, when the NMC sub-layer was relatively thick, the LFP sub-layer was again fully charged at the terminal voltage (473 s) but the overall electrode capacity was reduced because the 100% SOC LFP sub-layer was a small fraction of the overall electrode, and there was insufficient time to charge fully the higher capacity NMC sub-layer. In Fig. 13c, the LFP sub-layer reached a higher normalised maximum current density of 4.6 compared with 3.0 for the 50% case in Fig. 13b, potentially leading to reduced cycle lifetime when the LFP sub-layer is too thin.

The optimal case of 43% NMC sub-layer thickness provided the most favourable balance because (i) the high capacity but high resistance NMC sub-layer was in a position and proportion that

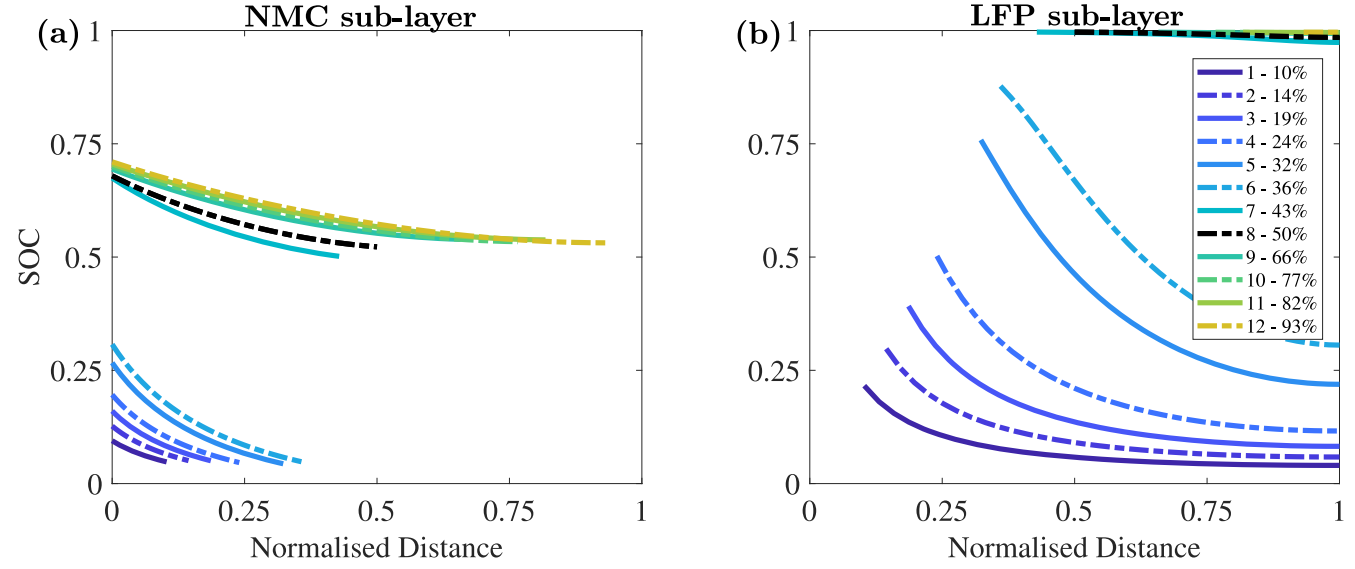

Figure 12. Simulated local state of charge (SOC) after a 4.5C charge at the terminal voltage of 4.2 V, as a function of position for (a) the NMC and (b) the LFP sub-layer. The different lines correspond to differing relative NMC sub-layer thicknesses with similar specific areal capacities, including the default 50:50 arrangement shown in black. The SOC was calculated from Eq. S4. The normalised distance from the separator is given by $(x - L_s)/(L_{p1} + L_{p2})$.

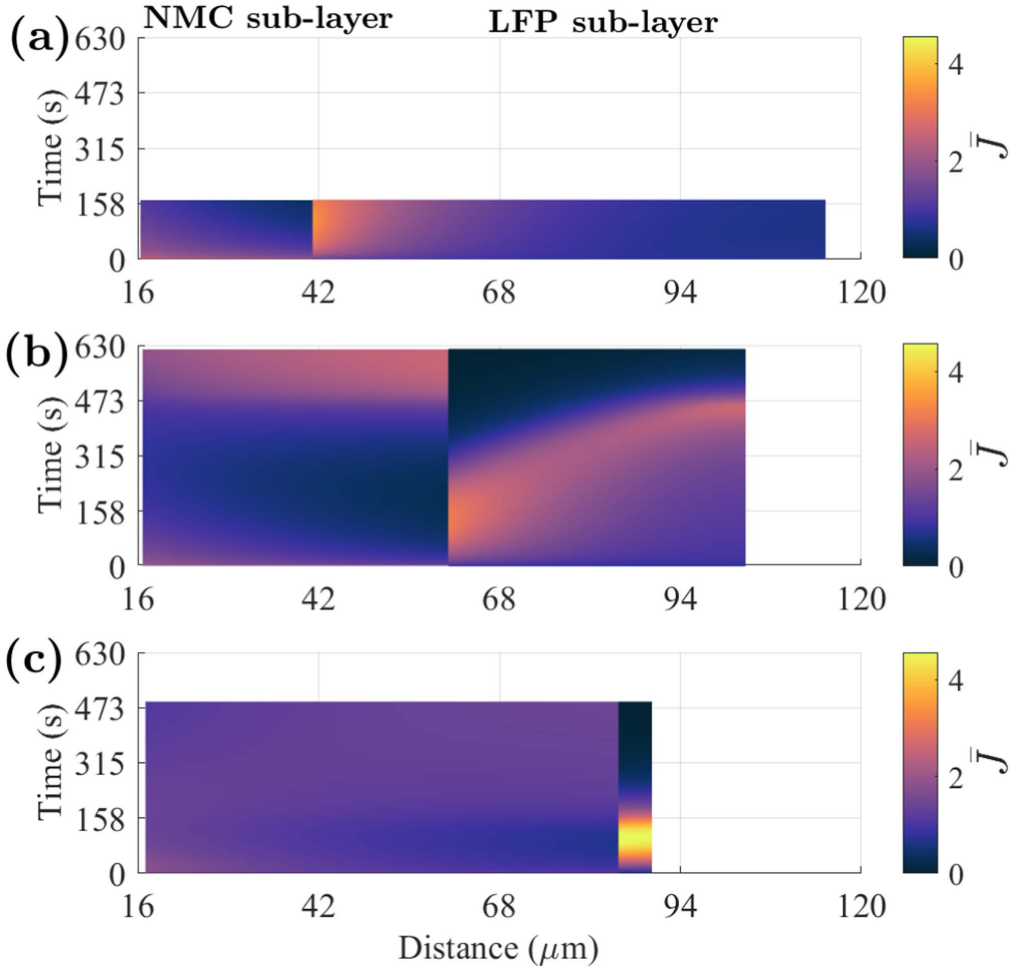

Figure 13. The normalised Butler-Volmer reaction current density ($\bar{J} = J_{\mathrm{p,i}}\ L\ a_{\mathrm{p,i}}/I$) as a function of distance from the counter electrode and time. Cases 4, 8 and 12 are shown in (a), (b), and (c), from Fig. 11, for a 4.5C charge. The separator is on the left and current collector is on the right.

ensured its charging time and contribution to overall capacity was maximised, even at fast charge, and (ii) the lower capacity but lower resistance LFP sub-layer was in a position and proportion to ensure that it finished charging to 100% SOC first, which in turn allowed the higher capacity NMC to charge for longer in a local environment where there were sufficient Li ions in the electrolyte. In summary:

1. When the LFP sub-layer was too thick, there was under utilization of both LFP and NMC and there was severe electrolyte depletion in the LFP sub-layer;
2. When the LFP sub-layer was too thin, it charged relatively quickly, but the overall capacity relied too much on the thick NMC sub-layer, which could not reach a high SOC before the cutoff voltage was reached; and
3. For the optimal case, the fraction of the lower capacity but fast to charge LFP was maximised, while ensuring sufficiently long overall charging times that maximised the contribution of the higher capacity NMC.

Taking experimental and modelling electrode performance as a whole, in regimes where local Li ion availability in the electrolyte is the capacity limiting factor for conventional electrodes, performance benefits can be realised by the use of novel, model-informed bilayer electrode designs. In the fast charge experiments and simulations here, the electrode is driven to 4.2 V, which is significantly beyond the plateau voltage of LFP of approximately 3.5 V where the majority of LFP charge storage occurs. In the bilayer and NMC electrodes, this is required to realize the significant capacity contributions from the NMC that charges at higher voltage. Although not studied in the current work, cyclic exposure of LFP to an over-voltage can be expected to lead progressive and irreversible changes in the LFP and an undermining of overall long-term capacity. On the other hand, electrolyte concentration plots, such as Fig. 7, are flattened for the bilayer electrode and suggest that high local concentration overpotentialsanother source of degradationmay be reduced for bilayer electrodes. For example, Fig. S9 shows the simulated electrolyte potential at the current collector as a function of time during a 3C charge. The maximum potential for the NMC-only and NMC sub-layer of the bilayer was similar, relatively low and nearly constant. In contrast, the potential for the LFP-only electrode increased dramatically in the final stages of charging whereas the electrolyte potential in the LFP sub-layer reduced in the final stages of charging, related to the different electrolyte concentration profile produced by layering (Fig. S7). A lower electrolyte potential reduces degradation.[38,39] The long-term net outcome of overcharging, reduced local concentration over-potentials and other effects due to layering are hard to anticipate in advance, and cycling behavior of layered electrodes is the subject of our future work.

The current work considers only the electrode dynamics in the positive electrode of a LIB. In a full cell arrangement closer to a practical LIB, the changes in the through-thickness Li concentration profile in the electrolyte that are induced in the positive electrode by a bilayer arrangement will also change the shape of the inter-linked Li concentration profile in the negative electrode. Conceptually these changes might be contrived by a graded or layered anode, or cathode

design, to minimize local electrochemical conditions that lead to Li plating in graphite anodes, which remains a widespread and performance limiting issue for LIBs. The flexible M-DFN model allows these and other ideas to be explored rapidly and is the focus of ongoing work. By combining this type of design-led approach to hetero-electrodes and cells with suitable electrode manufacturing innovations, it seems likely that batteries with previously unavailable combinations of properties may be realisable based on conventional and well-characterised materials.

Conclusions

We explored bilayer cathodes for a Li-ion battery by experiment and numerical simulation based on discrete sub-layers of NMC622 and LFP with the aim of designing an electrode constructed with conventional chemistries but which significantly improved charging capacity. We formulated a "Multilayer DFN" (M-DFN) model that simulated discrete sub-layers of different active materials for a LIB cathode. The M-DFN model readily simulated any distinct number of layers in both LIB positive or negative electrodes. We fitted the model to experimental data from a small number of LFP-only and NMC-only electrodes, and then also fitted and validated the model for a 50:50 NMC:LFP sub-layer thickness bilayer arrangement, over a range of charge and discharge rates. For the bilayer electrode, the open circuit potential functions of NMC and LFP played a key role in how the LFP and NMC active particles lithiated sequentially (LFP first for charge) at low C rates, or simultaneously at higher C rates. The model showed how electrode overall thickness, relative thickness of the sub-layers and open circuit potential influenced overall performance. In particular, the model revealed how electrode design controlled the spatial distribution of Li concentration in the electrolyte and the tendency for under utilization of active material, especially as significant gradients became established under certain conditions. At a 3C charge, the overall capacity of an optimised bilayer electrode could be increased by 5.6% and 6.3% over LFP-only or NMC-only electrodes, respectively. The bilayer electrode showed superior charging performance up to 4C because there was no Li electrolyte depletion anywhere through the bilayer thickness at any point in the charge cycle, and active particle utilization was therefore maximised.

Acknowledgments

Funding for this work was provided by the Faraday Institution through project "Nextrode—next generation electrodes" (Grant numbers: FIRG015 and FIRG066). RD acknowledges funding by a UKIC Research Fellowship from the Royal Academy of Engineering. YS acknowledges the use of characterization facilities and valuable discussion within the David Cockayne Centre for Electron Microscopy, Department of Materials, University of Oxford, alongside financial support provided by the Henry Royce Institute (Grant ref EP/R010145/1) and a David Cockayne Fellowship at Linacre College, University of Oxford.

Code Availability

The DFN simulation and post-processing codes that have been used to produce the results of this study are available as open-source code by author E. C. Tredenick (https://github.com/EloiseTredenick/DFN-P2D-Uniform-Matlab-NMC-LFP-LiIon-Batteries) and the M-DFN code will be available in the future. Please contact the corresponding author for more information.

ORCID

E. C. Tredenick https://orcid.org/0000-0001-9105-2858
S. Wheeler https://orcid.org/0000-0002-4503-4621
R. Drummond https://orcid.org/0000-0002-2586-1718
Y. Sun https://orcid.org/0000-0001-8661-8642
S. R. Duncan https://orcid.org/0000-0002-9525-7305
P. S. Grant https://orcid.org/0000-0002-7942-7837

References

1. "COP26 declaration: zero emission cars and vans," 2022, https://www.gov.uk/government/publications/cop26-declaration-zero-emission-cars-and-vans.
2. I. Hadjipaschalis, A. Poullikkas, and V. Efthimiou, *Ren Sust Energy R*, **13**, 1513 (2009).
3. B. Diouf and R. Pode, *Renewable Energy*, **76**, 375 (2015).
4. J. T. Frith, M. J. Lacey, and U. Ulissi, *Nature Comm*, **14**, 420 (2023).
5. P. S. Grant et al., *J. Phys. Energy*, **4**, 042006 (2022).
6. A. Yao, (2020), Enpower, https://www.enpowerinc.com/technology/white-papers/.
7. C. Cheng, R. Drummond, S. R. Duncan, and P. S. Grant, *J. Power Sources*, **413**, 59 (2019).
8. S. G. Marquis, V. Sulzer, R. Timms, C. P. Please, and S. J. Chapman, *J. Elect. Soc.*, **166**, A3693 (2019).
9. E. C. Tredenick, A. M. Boyce, S. Wheeler, J. Li, Y. Sun, R. Drummond, S. R. Duncan, P. S. Grant, and P. R. Shearing, (2024), (preprint), 10.21203/rs.3.rs-3639668/v1.
10. M.-H. Kim, M. Oh, H.-M. So, N. H. Hatsey, H.-J. Lee, and S. Hyun, *Adv. Funct. Mater.*, **33**, 2208665 (2023).
11. S. Kalnaus, K. Livingston, W. B. Hawley, H. Wang, and J. Li, *J. Energy Stor.*, **44**, 12 (2021).
12. R. Chowdhury, Y. Zhao, Y. Xia, M. Ouyang, N. Brandon, and A. Banerjee, *Sust. Energy Fuels*, **5**, 5193 (2021).
13. E. G. Sukenik, L. Kasaei, and G. G. Amatucci, *J. Power Sources*, **579**, 233327 (2023).
14. R. Drummond, C. Cheng, P. Grant, and S. Duncan, *J. Elect. Soc.*, **169**, 010528 (2022).
15. S. H. Lee, C. Huang, and P. S. Grant, *Nano Energy*, **61**, 96 (2019).
16. X. Lu et al., *Nat. Commun.*, **11**, 2079 (2020).
17. J. Whitacre, K. Zaghib, W. West, and B. Ratnakumar, *J. Power Sources*, **177**, 528 (2008).
18. T. L. Kirk, J. Evans, C. P. Please, and S. J. Chapman, *SIAM J. App. Math.*, **82**, 625 (2022).
19. E. Hosseinzadeh, J. Marco, and P. Jennings, *App. Math. Model*, **61**, 107 (2018).
20. V. Ramadesigan, R. N. Methekar, F. Latinwo, R. D. Braatz, and V. R. Subramanian, *J. Elect. Soc.*, **157**, A1328 (2010).
21. R. Chowdhury, A. Banerjee, Y. Zhao, X. Liu, and N. Brandon, *Sustainable Energy Fuels*, **5**, 1103 (2021).
22. M. Doyle, T. F. Fuller, and J. Newman, *J. Elec. Soc.*, **140**, 1526 (1993).
23. G. Richardson, I. Korotkin, R. Ranom, M. Castle, and J. M. Foster, *Elect. Acta.*, **339**, 135862 (2020).
24. I. Korotkin, S. Sahu, S. E. J. O'Kane, G. Richardson, and J. M. Foster, *J. Elect. Soc.*, **168**, 060544 (2021).
25. T. L. Kirk, C. P. Please, and S. J. Chapman, *J. Elect. Soc.*, **168**, 060554 (2021).
26. R. Xu, Y. Yang, F. Yin, P. Liu, P. Cloetens, Y. Liu, F. Lin, and K. Zhao, *J. Mech. Phys. Solids*, **129**, 160 (2019).
27. A. Jokar, M. Désilets, M. Lacroix, and K. Zaghib, *J. Power Sources*, **379**, 84 (2018).
28. H. Noh, S. Youn, C. S. Yoon, and Y. Sun, *J. Power Sources*, **233**, 121 (2013).
29. D. B. Newell et al., "The international system of units (SI)." *NIST Special Publication*, **330**, 1 (2019).
30. L. O. Valøen and J. N. Reimers, *J. Elect. Soc.*, **152**, A882 (2005).
31. MATLAB, version 9.13.0.2049777 (R2022b). Natick, Massachusetts: The MathWorks Inc. (2022), https://au.mathworks.com/ (MATLAB).
32. A. M. Boyce, E. Martínez-Pañeda, A. Wade, Y. S. Zhang, J. J. Bailey, T. M. Heenan, D. J. Brett, and P. R. Shearing, *J. Power Sources*, **526**, 231119 (2022).
33. M. Farkhondeh, M. Safari, M. Pritzker, M. Fowler, T. Han, J. Wang, C. Delacourt, J. J. Wang, and C. Delacourt, *J. Elect. Soc.*, **161**, A201 (2013).
34. J. Costard, M. Ender, M. Weiss, and E. Ivers-Tiffée, *J. Elect. Soc.*, **164**, A80 (2016).
35. M. Castle, G. Richardson, and J. M. Foster, *European J. App. Math.*, **33**, 328 (2022).
36. C. Heubner, M. Schneider, and A. Michaelis Adv, *Energy Mat.*, **10**, 1902523 (2020).
37. A. Zuo, R. Fang, Z. Wu, and Z. Li, *J. Energy Storage*, **56**, 105920 (2022).
38. R. Xu, Y. Yang, F. Yin, P. Liu, P. Cloetens, Y. Liu, F. Lin, and K. Zhao, *J. Mech. Phys. Solids*, **129**, 160 (2019).
39. J. S. Edge et al., *Phys. Chem. Chem. Phys.*, **23**, 8200 (2021).